Supporting information

Charge Transport and Trap State Engineering in Transition Metal-Doped Bismuth Vanadate Photoanodes: A DFT study

Balaji G. Ghule, Seung Gyu Gyeong, Ji-Hyun Jang*

School of Energy and Chemical Engineering, Department of Energy Engineering, Graduate School of Carbon Neutrality, Graduate School of Semiconductor Materials and Devices Engineering, Ulsan National Institute of Science and Technology,

Ulsan-44919, Republic of Korea

Email: clau@unist.ac.kr

Computational methods

The effective masses of electrons and holes were extracted from the electronic band structure using the following relation [1]:

$$\frac{1}{m^*} = \frac{1}{\hbar^2}\frac{d^2(E)}{dk^2} \quad (1)$$

where m^* is the effective mass (m_e), $\hbar$ is the reduced Planck constant (eV.s), and $\frac{d^2(E)}{dk^2}$ is the second derivative of the energy with respect to the wavevector, evaluated at the band extremum. The carrier mobilities of electrons and holes were estimated using the obtained effective masses and the Drude model [2]:

$$\mu = \frac{q\tau}{m^*} \quad (2)$$

where μ is the carrier mobility (cm²/V·s), q is the elementary charge, τ is the mean free time (assumed to be $1 \times 10^{-16} s$), and m^* is the effective mass. The carrier diffusion lengths were calculated using the following expression [3]:

$$L_D = \sqrt{D\tau} \quad (3)$$

where L_D is the diffusion length (nm), D is the diffusion coefficient, and τ is the carrier lifetime ($1 \times 10^{-8} s$), consistent with the recent findings of Song et al [4]. The diffusion coefficient D was calculated using the Einstein's relation:

$$D = \frac{\mu k_B T}{q} \quad (4)$$

where k_B the Boltzmann constant $(8.617 \times 10^{-5}\ eV/K)$, T the absolute temperature (K), and q the elementary charge.

The charge density difference, K-path for band structure calculations, and the energy levels of the conduction and valence bands were evaluated using the VASPKIT toolkit [5].

For further calculations, pure and doped (001) slab surfaces of BVO were constructed using a fully relaxed cell. The surfaces of the pure and doped BVO contained four-layered slabs, with each slab composed of 48 atoms. A vacuum layer of at least 15 Å was added to avoid interactions between periodic layers. The lower two layers of the slab were fixed, while the upper two layers were fully relaxed. A Monkhorst-Pack k-point mesh of 3 × 3 × 1 was used for Brillouin zone sampling and total energy calculations.

The formation energies of the doped BVO were calculated as follows [6]:

$$E_{F(M-doped)} = E_{(M-doped)} - E_{(pure)} - \mu_M + \mu_{Fe} \quad (5)$$

where, $E_{(pure)}$, *and* $E_{(M\text{-}doped)}$, are the obtained energies for pure, and M-doped BVO, respectively. μ_M, and μ_{Fe} are the chemical potentials of doped metal, and Fe, respectively.

The Gibbs free energy for each intermediate step was calculated as [7]:

$$\Delta G = \Delta E_{(DFT)} + (ZPE - \Delta TS) - e.U \quad (6)$$

where ΔE, is the change in adsorption energy, *ZPE is* the zero-point energy, *T* is the temperature (298.15 K), S is the entropy, *e* is the electronic charge and *U* is the applied electrode potential. The ZPE was obtained by post-processing the vibrational energy calculations using VASPKIT toolkit. At standard condition with U = 0, the highest free energy is equal to the reaction potential for electrochemical reaction and $(\Delta G_{max} - 1.23)$ is equal to overpotential.

$$\Delta G_{max} = (\Delta G_1, \Delta G_2, \Delta G_3, \Delta G_4) \quad (7)$$

In alkaline media, the OER reaction process occurs as follows:

$$\Delta G_1 = \ * \ + \ OH^- \rightarrow HO^* + e^- \quad (8)$$

$$\Delta G_2 = HO^* + OH^- \rightarrow O^* + e^- \quad (9)$$

$$\Delta G_3 = O^* + OH^- \rightarrow HOO^* + e^- \quad (10)$$

$$\Delta G_4 = HOO^* + OH^- \rightarrow O_2 + e^- + *$$ (11)

The theoretical reaction overpotential (η) is calculated using following equation:

$$\eta = \frac{(\Delta G_{max})}{e} - 1.23$$ (12)

where, ΔG_{max} is the largest potential difference step in the OER reaction step.

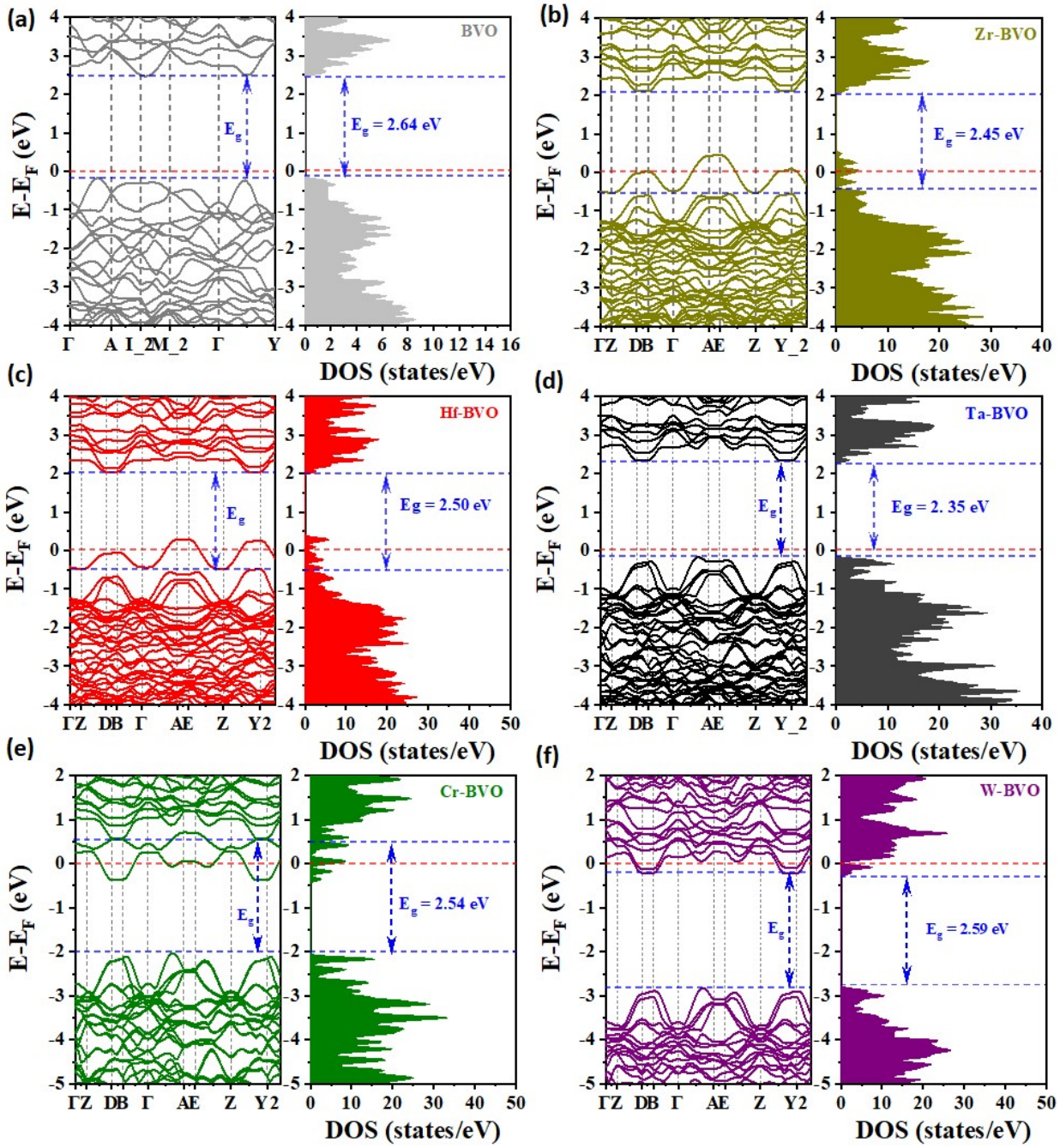

Figure S1: DFT-calculated band structure of (a) pure; (b) Zr^{4+} doped, (c) Hf^{4+} doped, (d) Ta^{5+} doped, (e) Cr^{6+} doped, and, (f) W^{6+} doped BVO, respectively. The blue dashed lines represent CBM/VBM, red dashed lines represent fermi level (E_f).

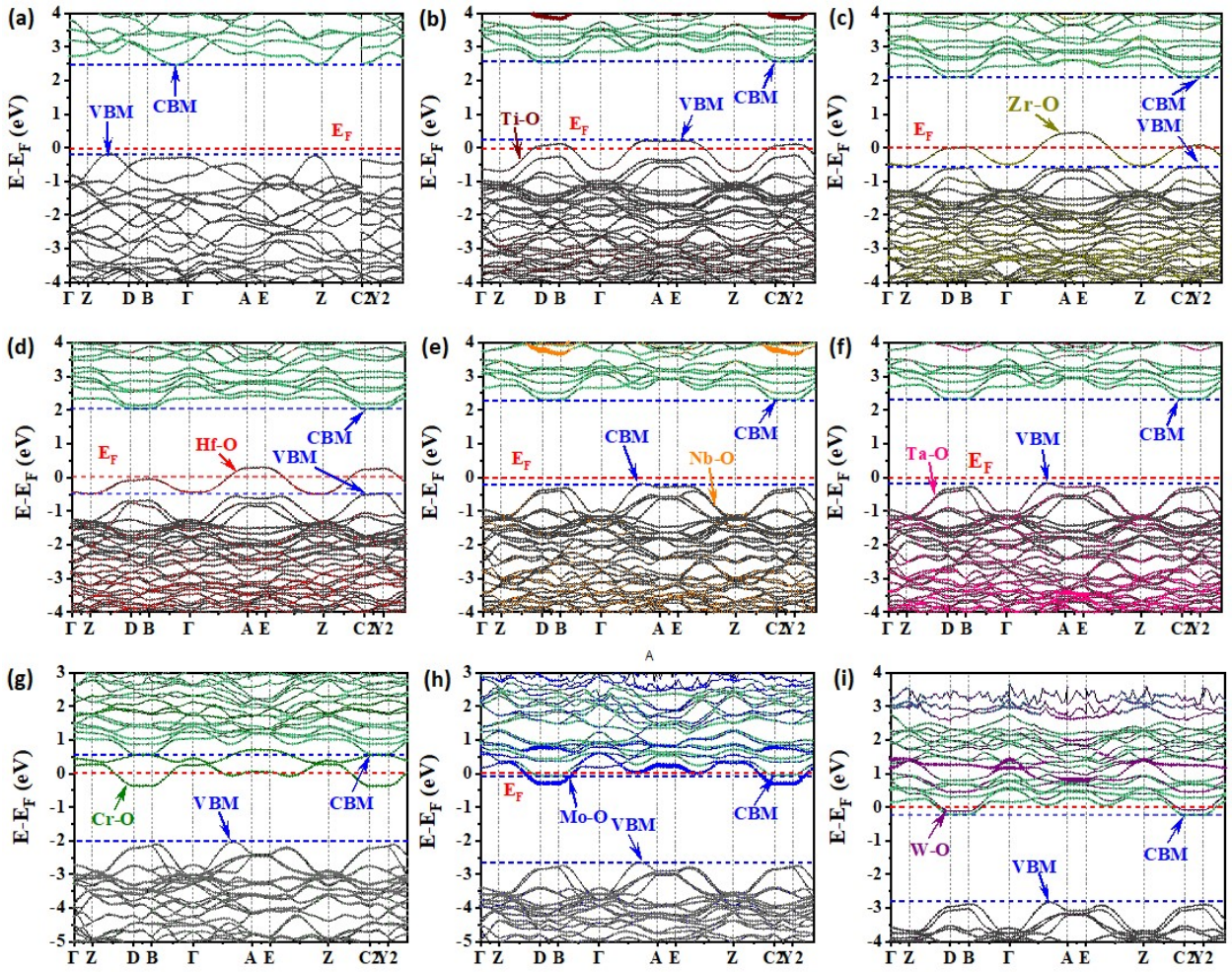

Figure S2: DFT-calculated projected band structure of (a) pure; (b) Ti^{4+} doped, (c) Zr^{4+} doped, (d) Hf^{4+} doped, (e) Nb^{5+} doped, (f) Ta^{5+} doped, (g) Cr^{6+} doped, (h) Mo^{6+} doped and, (i) W^{6+} doped BVO, respectively. The blue dashed lines represent CBM/VBM, red dashed lines represent fermi level (E_F).

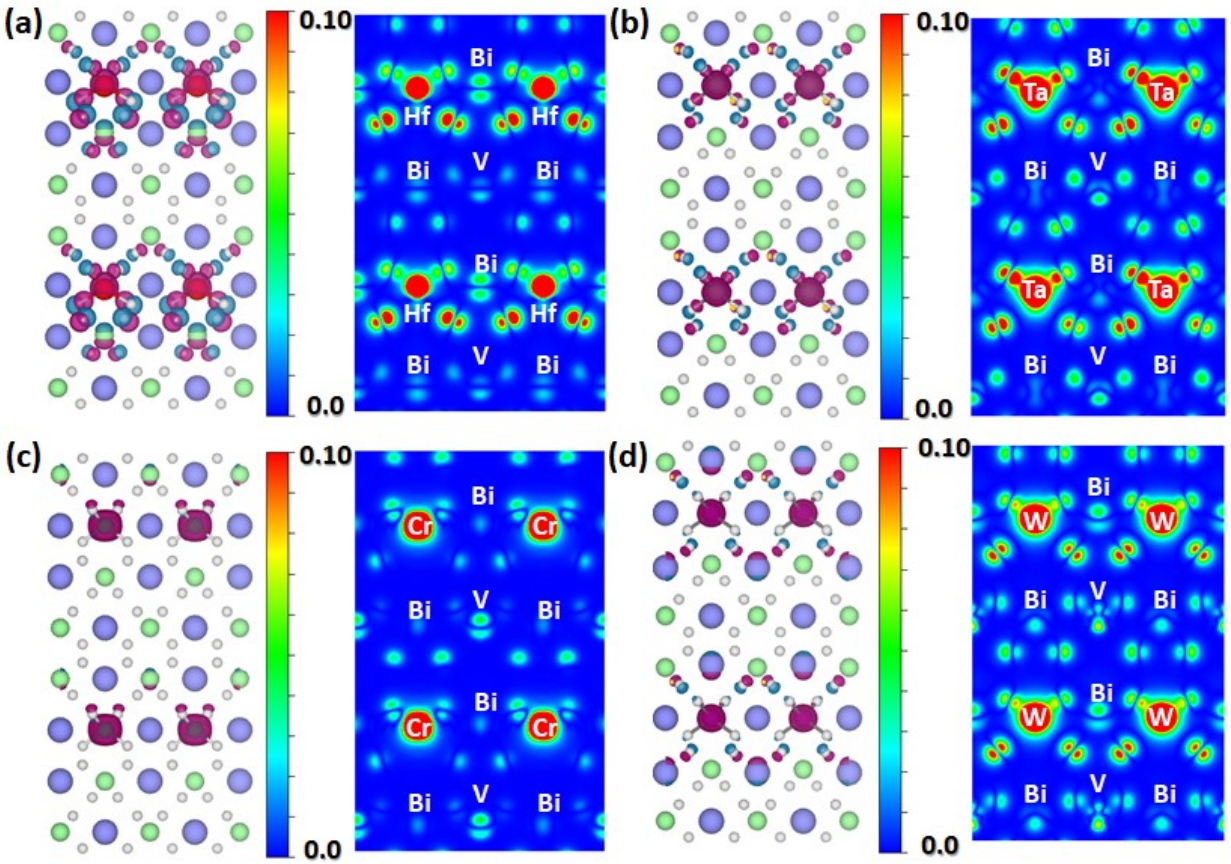

Figure S3: DFT-calculated charge density difference and 2D-charge density maps along (001) plane of a) Hf-doped; b) Ta-doped, c) Cr- doped, and d) W- doped BVO, respectively. The iso-surface value was set to 0.05 eV/Å^3. The dark-cyan and purple color regions represent the charge accumulation and depletion respectively. The red and blue regions in 2D-charge density map represent the higher and lower charge regions, respectively.

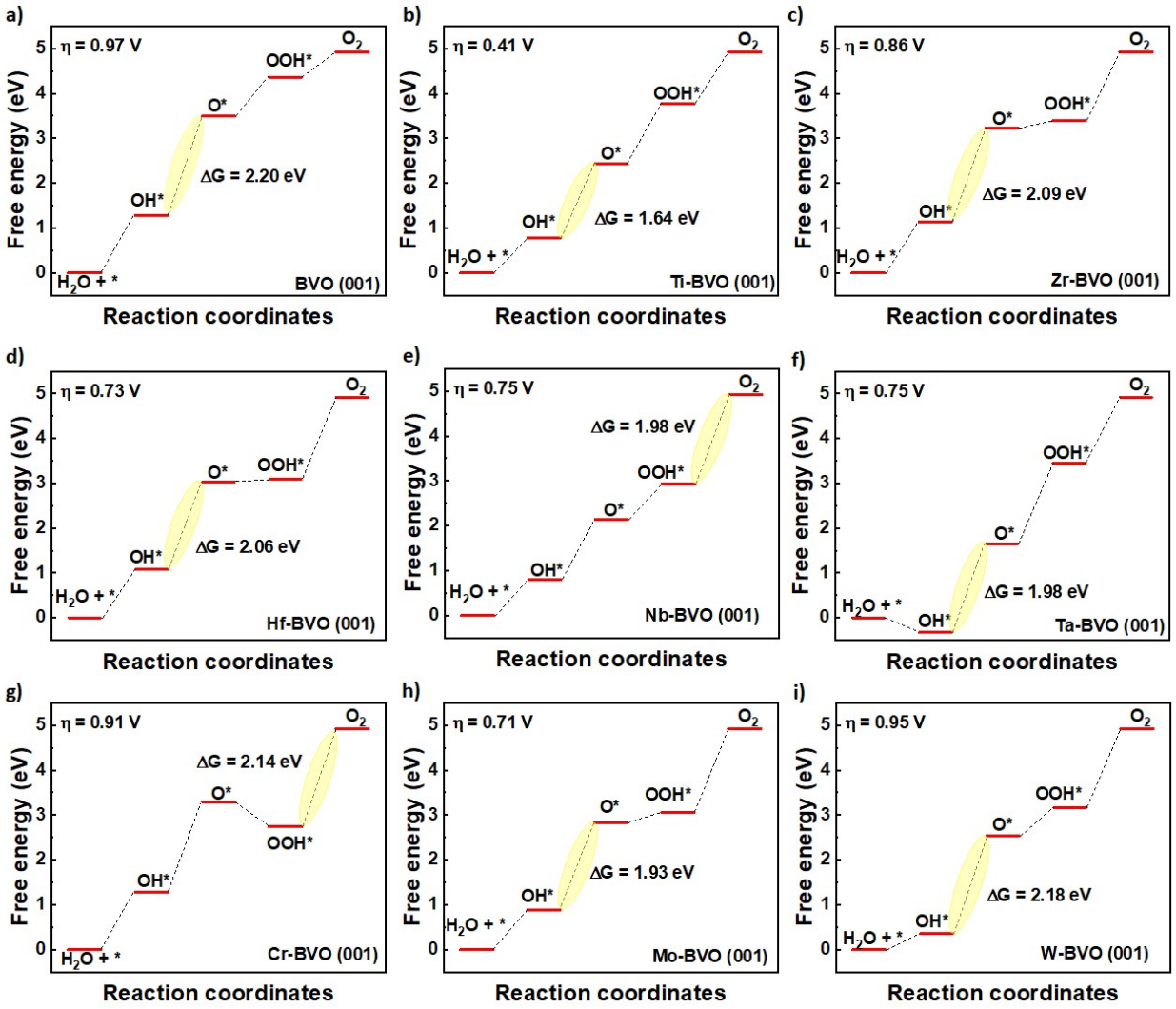

Figure S4: Calculated Gibbs free energies of pure and doped BVO at 0 V potential. The light-yellow highlighted region represents the PDS for each sample.

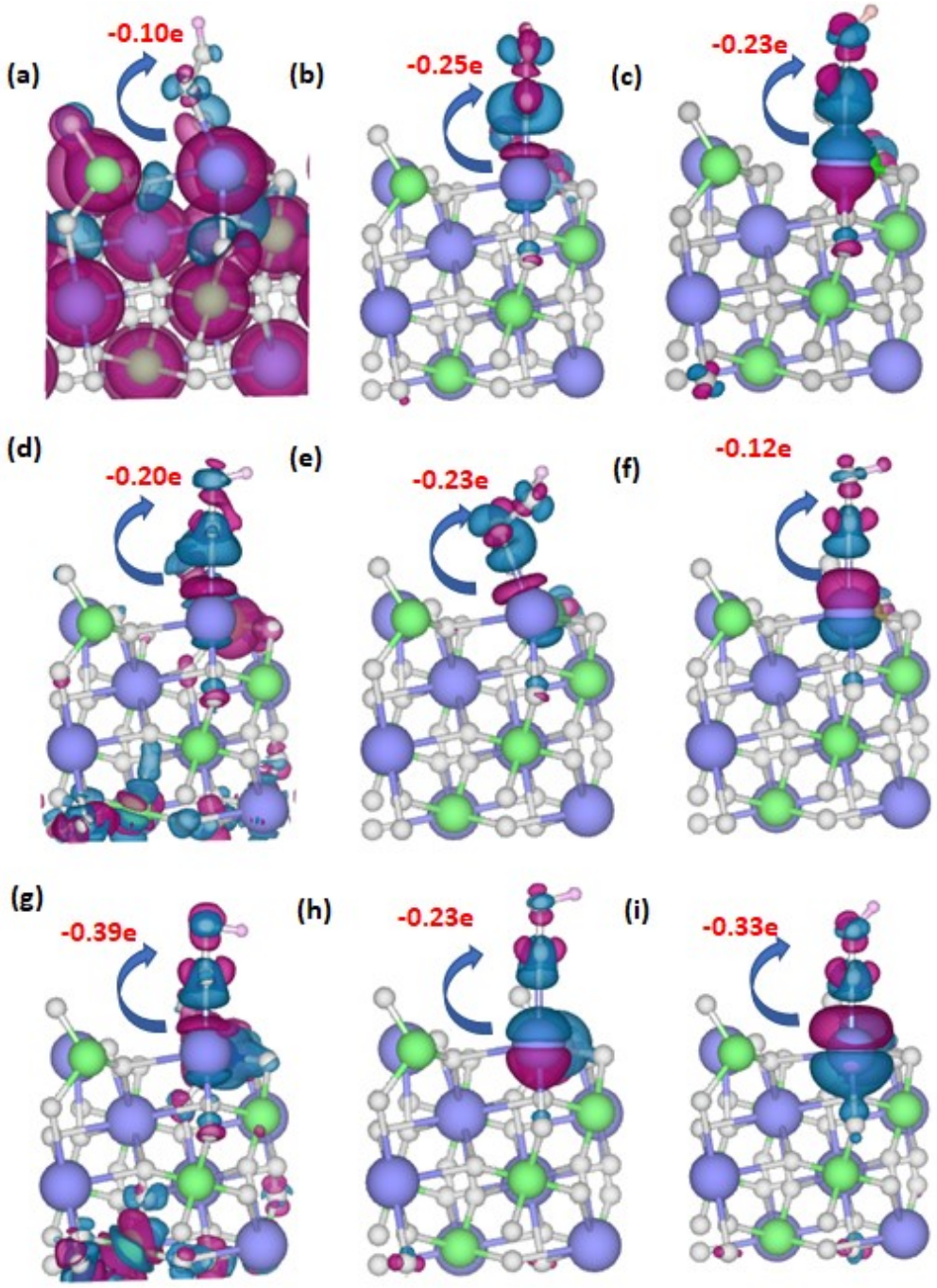

Figure S5: DFT-calculated charge density difference of OOH_{ads} on (001) surfaces of (a) pure; (b) Ti^{4+} doped, (c) Zr^{4+} doped, (d) Hf^{4+} doped, (e) Nb^{5+} doped, (f) Ta^{5+} doped, (g) Cr^{6+} doped, (h) Mo^{6+} doped and, (i) W^{6+} doped BVO, respectively. The dark-cyan and purple color represent the charge accumulation and depletion respectively. The blue, green, grey, and light-pink balls represent Bi, V, O, and H atoms respectively.

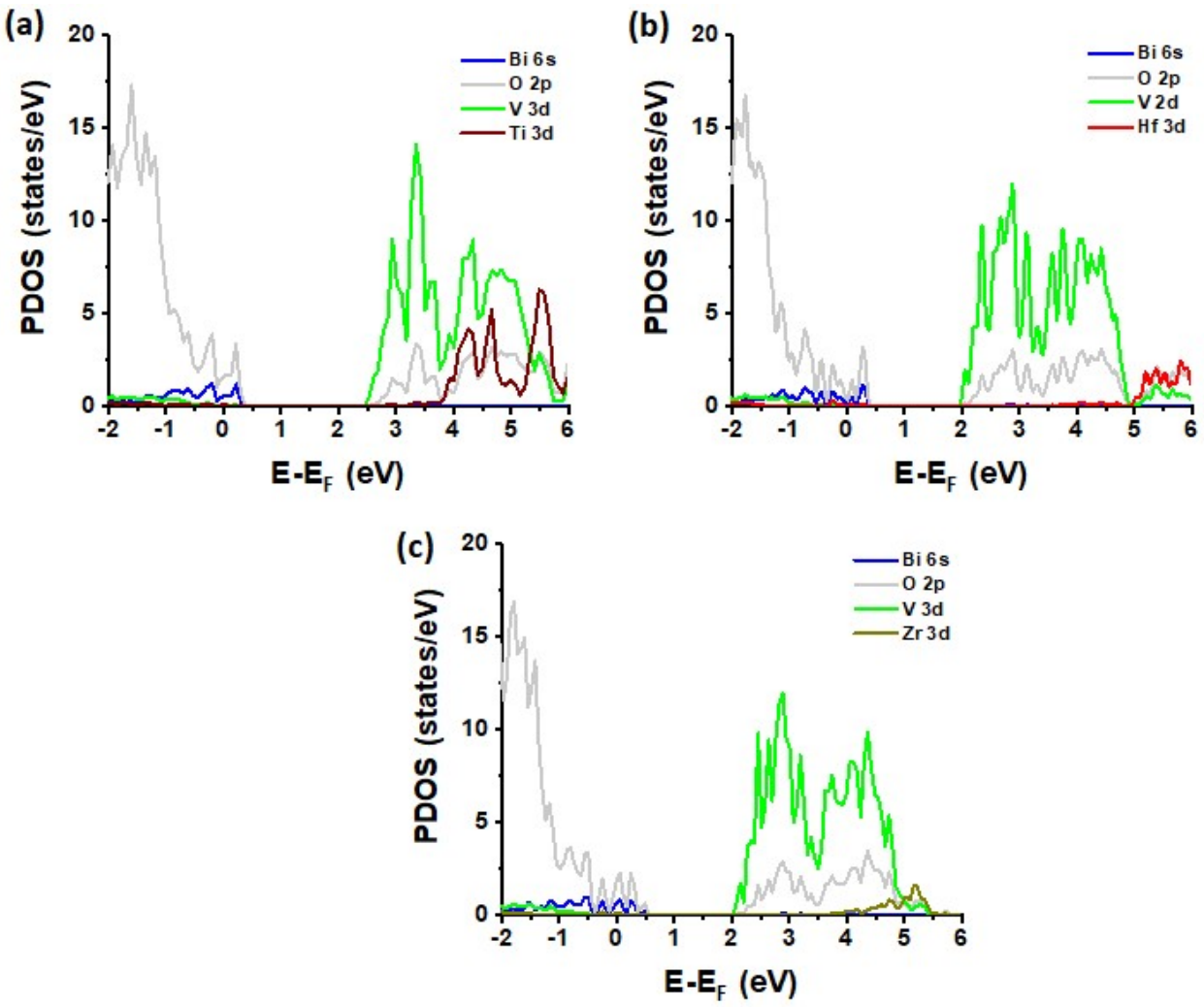

Figure S6: DFT-calculated projected density of states of (a) Ti^{4+} doped, (b) Hf^{4+} doped, (c) Zr^{4+} doped BVO, respectively.

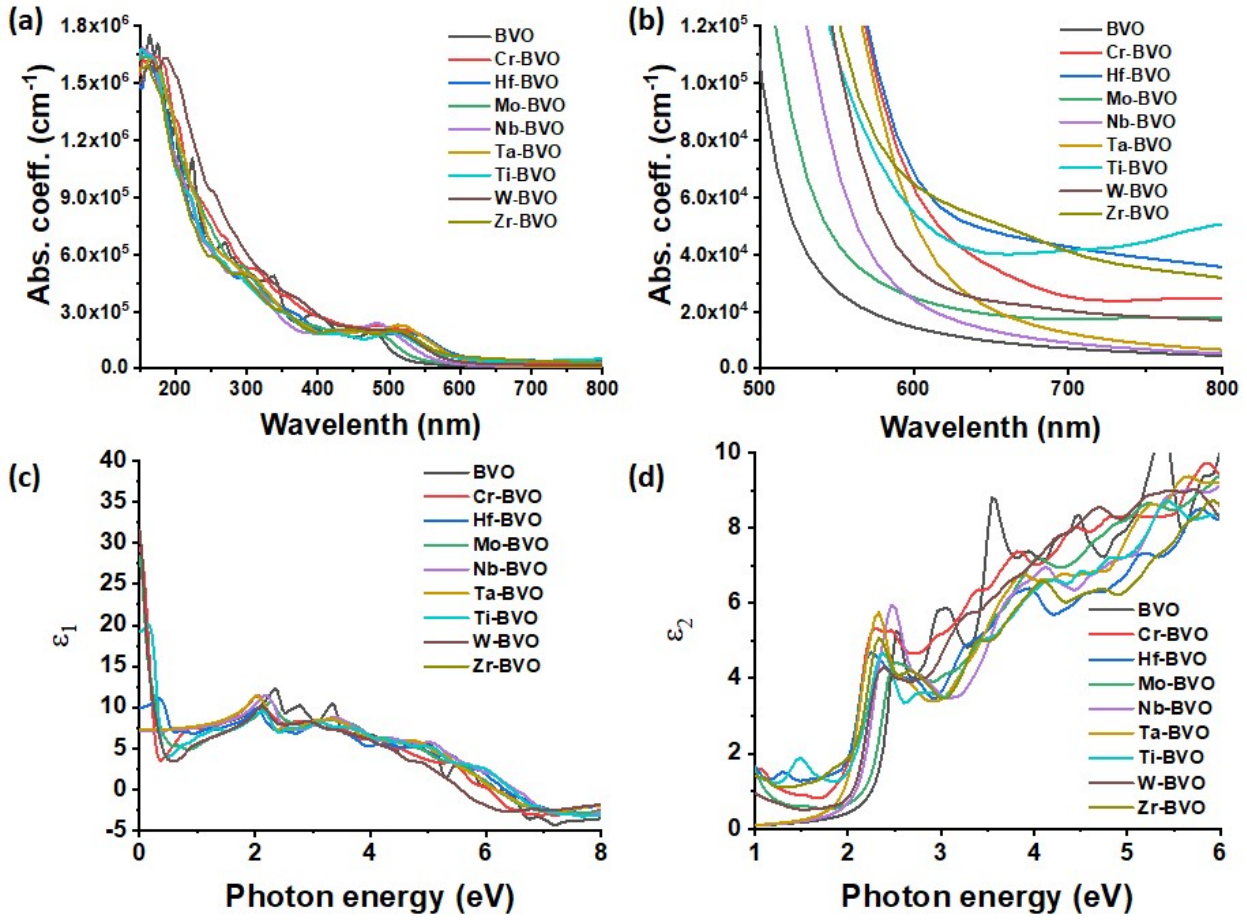

Figure S7: DFT-calculated optical properties of pure and doped BVO: (a) absorption spectra, (b) magnified absorption spectra, (c) real part of dielectric constant and (d) imaginary part of dielectric constant.

Table S1: The optimized adsorbate bond lengths and bond angles for OH adsorbed on the pristine and doped BVO.

Photoanode	**OH* adsorbed on the surface**	
	Bond length (Å)	**Bond angle (°)**
	Bi-O	**Bi-OH**
BVO	2.10	109.94
Ti-BVO	2.18	136.75
Hf-BVO	2.41	158.12
Zr-BVO	2.18	114.70
Ta-BVO	2.11	112.36
Nb-BVO	2.15	109.92
Cr-BVO	2.47	138.98
Mo-BVO	2.18	114.70
W-BVO	2.18	114.70

Table S2: Comparison of obtained carrier mobility and overpotentials of Ti, Mo, and W-doped $BiVO_4$ with the previously reported work.

Photoanode	**Carrier mobility ($cm^2 V^{-1} S^{-1}$)**	**Overpotentials (η) (V)**	**Reference**
Ti-BVO	-	0.44	8
Ti-BVO	-	0.97	9
Mo-BVO	1.07×10^{-4}	-	10
Mo-BVO	-	0.54	11
W-BVO	5×10^{-5}	-	12
W-BVO	2.2×10^{-4}	-	13
Mo-BVO	-	0.79	14
W-BVO	-	1.50	14
Ti-BVO	1.5×10^{-5}	**0.41**	**This work**
Mo-BVO	9.31×10^{-6}	**0.71**	**This work**
W-BVO	9.31×10^{-6}	**0.95**	**This work**

References:

1. Green, M. A., Intrinsic concentration, effective densities of states, and effective mass in silicon, *J. Appl. Phys.*, **1990**, *67*, 2944–2954.
2. Whalley, L. D.; Frost, J. M.; Morgan, B. J.; Walsh, A., Impact of nonparabolic electronic band structure on the optical and transport properties of photovoltaic materials, *Phys. Rev. B*, **2019**, *99*, 085207.
3. Hodes, G.; Kamat, P. V., Understanding the implication of carrier diffusion length in photovoltaic cells, *J. Phys. Chem. Lett.*, **2015**, *6*, 4090–4092.
4. Kwon, J., Choi, H., Choi, S., Sun, J., Han, H., Paik, U., Choi, J. and Song, T., 2025. Improved Charge Carrier Dynamics by Unconventional Doping Strategy for BiVO4 Photoanode. *Small Science*, p.2500051.
5. Wang, V.; Xu, N.; Liu, J. C.; Tang, G.; Geng, W. T., VASPKIT: A user-friendly interface facilitating high-throughput computing and analysis using VASP code, *Comput. Phys. Commun.*, **2021**, *267*, 108033.
6. J. Liu, Y. Jia, L. Ji, S. Bandaru, G. Bai, K. K. Cheepurupalli, X. Zhang, J. Phys. Chem. C 2023, 127, 8342.
7. J. Rossmeisl, Z. W. Qu, H. Zhu, G. J. Kroes, J. K. Nørskov, J. Electroanal. Chem. 2007, 607, 83.
8. Zhao, X., Hu, J., Wu, B., Banerjee, A., Chakraborty, S., Feng, J., Zhao, Z., Chen, S., Ahuja, R., Sum, T.C. and Chen, Z., 2018. Simultaneous enhancement in charge separation and onset potential for water oxidation in a $BiVO_4$ photoanode by W–Ti codoping. *Journal of Materials Chemistry A*, *6*(35), pp.16965-16974.
9. Zhang, T., Chen, M., Zhu, X. and Lin, P., 2025. A novel Ti-doped BiVO4 photoanode with NiFeOx cocatalyst for fast charge transfer towards enhanced photoelectrochemical water oxidation. *International Journal of Hydrogen Energy*, *107*, pp.469-477.

10. Wu, F. and Ping, Y., 2018. Combining Landau–Zener theory and kinetic Monte Carlo sampling for small polaron mobility of doped BiVO 4 from first-principles. *Journal of Materials Chemistry A*, *6*(41), pp.20025-20036.
11. Gutkowski, R., Masa, J. and Schuhmann, W., 2019. A combinatorial approach for optimization of oxygen evolution catalyst loading on Mo-Doped BiVO4 Photoanodes. *Electroanalysis*, *31*(8), pp.1500-1506.
12. Rettie, A.J., Chemelewski, W.D., Lindemuth, J., McCloy, J.S., Marshall, L.G., Zhou, J., Emin, D. and Mullins, C.B., 2015. Anisotropic small-polaron hopping in W: BiVO4 single crystals. *Applied Physics Letters*, *106*(2).
13. Abdi, F.F., Firet, N. and van de Krol, R., 2013. Efficient BiVO4 thin film photoanodes modified with Cobalt Phosphate catalyst and W-doping. *ChemCatChem*, *5*(2), pp.490-496.
14. Liu, T., Liu, R., Li, Q. and Yang, J., 2020. Theoretical insight into the role of defects and facets in the selectivity of products in water oxidation over bismuth vanadate (BiVO4). *ACS Sustainable Chemistry & Engineering*, *8*(4), pp.1980-1988.